JACS Au
AN OPEN ACCESS JOURNAL OF THE AMERICAN CHEMICAL SOCIETY

pubs.acs.org/jacsau

Article

Singlet Oxygen Generation from Polyaminoglycerol by Spin-Flip-Based Electron Transfer

Jung Seung Nam,[‖] Youngjoo Hong,[‖] Chae Gyu Lee,[‖] Tae In Kim,[‖] Chaiheon Lee, Deok-Ho Roh, In Seong Lee, Songa Kweon, Gyunhyeok Ahn, Seung Kyu Min,* Byeong-Su Kim,* and Tae-Hyuk Kwon*

Cite This: *JACS Au* 2022, 2, 933–942

Read Online

ACCESS | Metrics & More | Article Recommendations | Supporting Information

ABSTRACT: Reactive oxygen species have drawn attention owing to their strong oxidation ability. In particular, the singlet oxygen ($^1O_2$) produced by energy transfer is the predominant species for controlling oxidation reactions efficiently. However, conventional $^1O_2$ generators, which rely on enhanced energy transfer, frequently suffer from poor solubility, low stability, and low biocompatibility. Herein, we introduce a hyperbranched aliphatic polyaminoglycerol (hPAG) as a $^1O_2$ generator, which relies on spin-flip-based electron transfer. The coexistence of a lone pair electron on the nitrogen atom and a hydrogen-bonding donor (the protonated form of nitrogen and hydroxyl group) affords proximity between hPAG and O_2. Subsequent direct electron transfer after photo-irradiation induces hPAG$^{\bullet+}$-$O_2^{\bullet-}$ formation, and the following spin-flip process generates $^1O_2$. The spin-flip-based electron transfer pathway is analyzed by a series of photophysical, electrochemical, and computational studies. The $^1O_2$ generator, hPAG, is successfully employed in photodynamic therapy and as an antimicrobial reagent.

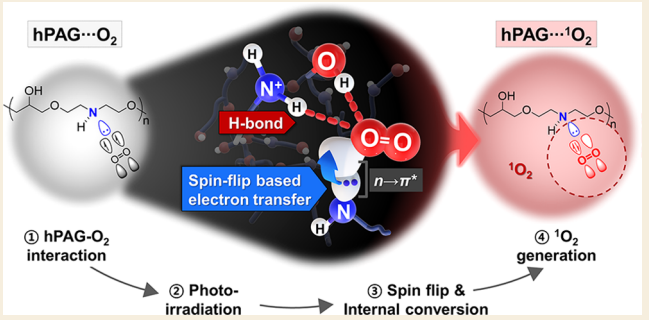

KEYWORDS: *spin-flip-based electron transfer, aliphatic polymer, O_2 interaction, singlet oxygen, photosensitizer, photodynamic therapy, antimicrobial reagents*

1. INTRODUCTION

Photosensitizer (PS)-mediated reactive oxygen species (ROS) generation has drawn significant attention owing to its extensive applications in various avenues such as photodynamic therapy, wastewater purification, antimicrobials, and photocatalytic organic synthesis.[1−8] Generally, ROS can be generated via two pathways: electron transfer (type I) or energy transfer (type II). Most oxygen radical anions, such as the superoxide radical ($O_2^{\bullet-}$) and hydroxyl radical ($OH^{\bullet}$), are generated through electron transfer from an electron donor, whereas singlet oxygen ($^1O_2$) is generated through energy transfer from the triplet state of a photosensitizer.[6,9−12] $^1O_2$ is a predominant species among the ROS and is a powerful oxidant.[8,12] To accomplish efficient $^1O_2$ generation, effective intersystem crossing (ISC) from singlet state to triplet state must be realized.[13,14] The ISC can be enhanced by increasing the coupling intensity ($T_n|\hat{H}_{SO}|S_1$) or decreasing the energy gap ($\Delta E_{S_1-T_n}$) between the S_1 and T_n states. Therefore, strategies based on the utilization of heavy atoms to increase the spin−orbit coupling constant and on intramolecular donor−acceptor charge separation to reduce $\Delta E_{S_1-T_n}$ have been explored.[14−17] However, photosensitizers based on these principles suffer from dark toxicity, poor solubility, and low stability. In addition, the energy transfer is strongly dependent on the distance between the donor and the acceptor, rendering the estimation of its efficiency highly challenging due to the mobility of O_2 (Scheme 1a).[18,19]

Herein, we report a molecular design strategy for $^1O_2$ generation via spin-flip-based electron transfer. This pathway harnesses the nitrogen lone pair−O_2−hydrogen-bonding interaction to minimize the distance between the photosensitizer and O_2 (Scheme 1b). Initially, we chose an amine group as the target functional moiety because of the interaction between the π^* orbitals of O_2 and the lone pair of N, which facilitates the chemical adsorption of O_2.[20,21] This is also the first step in the activation of O_2 in the oxygen reduction reaction (ORR).[20,21] Furthermore, we considered the hydrogen bonding with protonated amine and hydroxyl groups ($-NH_2^+-$ and $-OH$) as the additional factor for the strong affinity with O_2. Taken together, we developed a polyaminoglycerol (hPAG) as a

Received: January 26, 2022
Revised: March 15, 2022
Accepted: March 15, 2022
Published: March 29, 2022

https://doi.org/10.1021/jacsau.2c00050
JACS Au 2022, 2, 933−942

Scheme 1. Design Strategy and Mechanism of Electron Transfer-Mediated $^1O_2$ Generation by Photosensitizers[a]

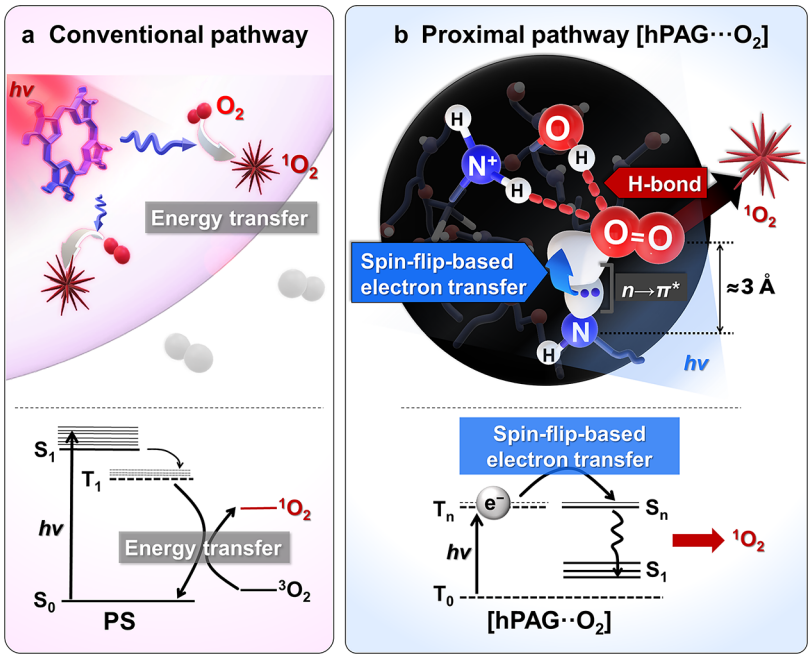

[a](a) $^1O_2$ generation based on "energy transfer" in conventional photosensitizers (PSs). (b) $^1O_2$ generation based on "spin-flip-based electron transfer" in rationally designed polyaminoglycerol (hPAG). Nonbonding lone pair of hPAG (blue) interacts with O_2 (red) within ~3 Å. Simultaneously, hydrogen-bonding donors of hPAG increase the affinity to O_2.

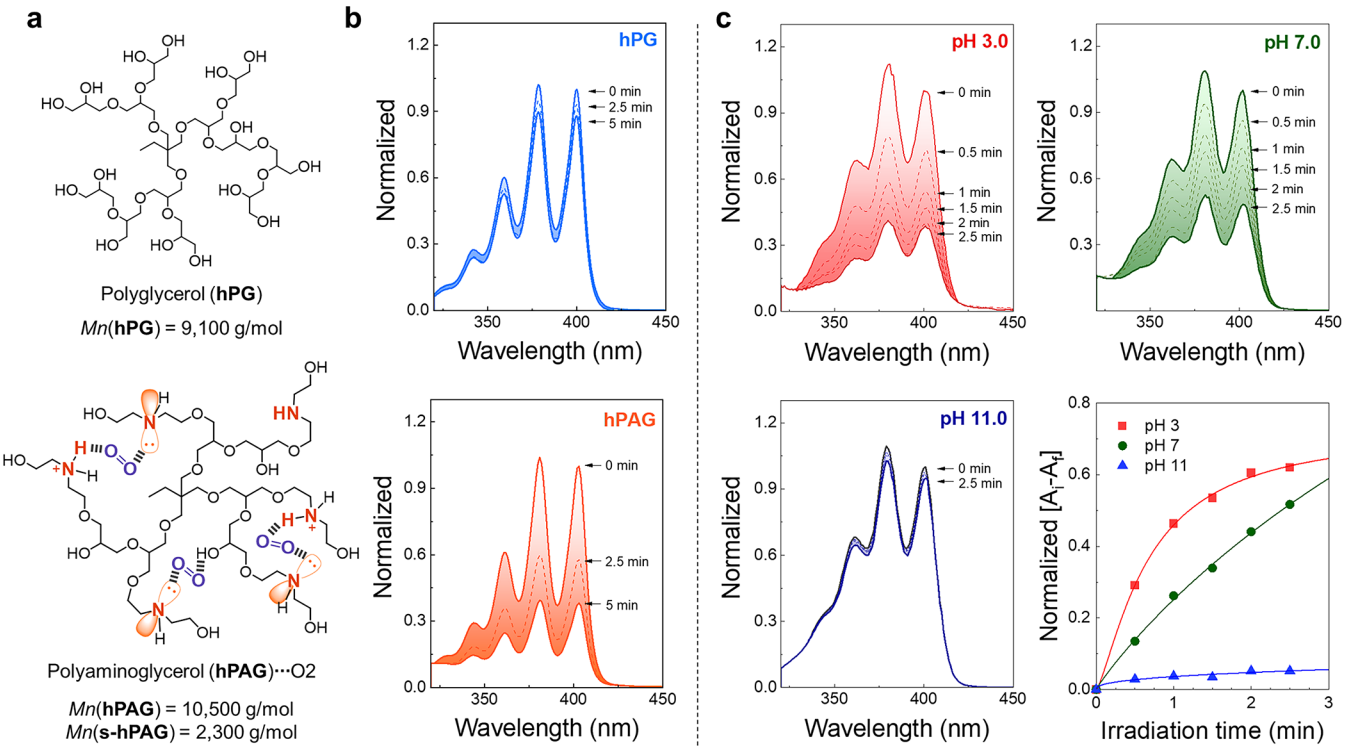

Figure 1. Identification of $^1O_2$ generation and its pH dependency. (a) Chemical structure of hyperbranched polyglycerol (hPG; top) and polyaminoglycerol (hPAG; bottom) interacting with O_2. (b) Validation of $^1O_2$ generation by utilizing 9,10-anthracenediyl-bis(methylene) dimalonic acid (ABDA). Absorbance of ABDA is attenuated after the reaction with $^1O_2$. Conditions [hPG or hPAG] = 10 μM, [ABDA] = 100 μM, irradiation power = 12.5 mW/cm^2. (c) Tracking the $^1O_2$ generation by hPAG at different pHs. The pH was adjusted using 1 mM NaOH and HCl. Conditions: [hPAG] = 10 mM, [ABDA] = 100 mM, light source = solar simulator, irradiation power = 25 mW/cm^2.

$^1O_2$ generator, which includes the N atom within the framework of the highly biocompatible hyperbranched polyglycerol (hPG) molecule. As a result, we found that O_2 was encapsulated within ~3 Å in the polymer network by the virtue of the (i) interaction between O_2 and the lone pair of N and (ii) hydrogen bonding (Scheme 1b). The polymer network allows direct electron

https://doi.org/10.1021/jacsau.2c00050
JACS Au 2022, 2, 933−942

transfer from the polymer to O_2 upon photo-irradiation, suggesting spin-flip-based electron transfer mechanism for $^1O_2$ generation. This is completely different from the conventional strategies for developing triplet photosensitizers (Scheme 1). The ROS generated was investigated by various methods and successfully utilized to exert oxidative stress, triggering photo-induced cancer cell death and antimicrobial effect. This approach provides new insights into the design strategy for improving the dark toxicity, water solubility, and stability of photosensitizers.

2. RESULTS AND DISCUSSION

2.1. Characterization of Synthesized hPAG

We first prepared Boc-protected aminoethanol glycidyl ether monomer (BAG) to synthesize hyperbranched hPAG, based on hPG backbone.[22] Owing to the unique three-dimensional architecture of hyperbranched hPG, which comprises a polyether backbone with several hydroxyl functional groups and exhibits excellent biocompatibility, it has gained significant attention in biological and biomedical applications. The Boc-protected hPAG was prepared by anionic ring-opening multi-branching polymerization using trimethylolpropane as an initiator in the presence of potassium methoxide (Figure S1). Then, deprotection was carried out with 1 M HCl to yield the desired hPAGs. To examine the ROS generation capability as a function of the number of nitrogen atoms in the polymeric backbone, the molecular weight of each polymer was controlled by adjusting the monomer-to-initiator ratio (hPAG, 10,500 g/mol; small hPAG (s-hPAG), 2,300 g/mol) (Figure 1a, bottom and Figure S2). Parallelly, the control hyperbranched hPG containing only O atoms in the backbone was prepared by following an identical protocol using glycidol as a monomer (Figure 1a, top and Figure S2). The hyperbranched architecture of the synthesized polymers was confirmed, with the degree of branching being 0.40−0.55 (Figure S3). The characterization data and details of all polymers including their molecular weight, degree of branching, and photostability are provided in the Supporting Information (Figures S2−S4).

The photophysical properties of hPG, s-hPAG, and hPAG were analyzed by ultraviolet−visible (UV−vis) (Figure S5) and photoluminescence (PL) spectroscopy (Figure S6). Interestingly, s-hPAG and hPAG exhibited an absorption band in the range of 250−450 nm (approximately 2.8−4.9 eV), whereas hPG exhibited no absorption in the same range. hPAG, with a higher molecular weight, exhibited stronger absorption than the corresponding s-hPAG, which implied that this absorption originated from the polymer network of hPAG. Moreover, the forbidden phosphorescence (PL) emission of the heavy-atom-free hPAG polymer could be observed at a low temperature of 77 K, which suppresses the nonradiative process by establishing an environment in which molecular motion is frozen. The following phosphorescence of hPAG was observed in the range of 400−500 nm (Figure S6), while no significant emission was observed in the same range of hPG (Figure S7). In addition, the phosphorescence of hPAG was quenched under O_2 bubbling compared to Ar bubbling (Figure S7a). Quenching by O_2 implies that the low-temperature PL emission of hPAG is derived from the triplet state. In contrast, no change of emission intensity was observed in the PL spectra of hPG under O_2 bubbling (Figure S7b).

This intrinsic optical property might originate from the nanocluster formed through hydrogen bond or electrostatic interactions in the branched polymer network.[23,24] In addition, the pH-titration curve of hPAG revealed the protonation behavior of hPAG in an aqueous solution (Figure S8). The titration curve of hPAG shows buffered region from polymer network showing variable pK_a values for secondary amine-like branched PEI.[25−27] This behavior is attributed to the hydrogen bonding between nitrogen lone pair and hydroxyl group or protonated amine in the hyperbranched hPAG network. Based on the results, it can be concluded that the optical properties of hPAG, endowed by the interactions in the polymer network, facilitate the utilization of its excited state, which can initiate photo-induced electron transfer from the lone pair of N to an appropriate target receiving its electron near the polymer. Considering various examples, where the N atom in PEI interacts with the O atom of a DNA strand or where N atom insertion on the edge of graphene enables O_2 adsorption, the optical properties of hPAG, engendered by the hyperbranched polymer architecture with an additional amine group, have prompted us to investigate the interaction of hPAG with O_2 and the following electron transfer to produce ROS after photo-activation.

2.2. Investigation of ROS Generation

We investigated the ROS generation ability of the compounds using three representative methods: dihydrorhodamine 123 (DHR123) assay for type I ROS,[28,29] 9,10-anthracenediyl-bis(methylene) dimalonic acid (ABDA) assay for $^1O_2$,[28,30] and electron paramagnetic resonance (EPR) spectroscopy with spin trapping.[32−34] The enhanced emission from DHR123 after photo-activation supports type I ROS generation by electron transfer, with yields decreasing in the order hPAG > s-hPAG > hPG (Figure S9). To confirm the generation of superoxide radical ($O_2^{\bullet-}$), we obtained EPR signals using 5,5-dimethyl-1-pyrroline N-oxide (DMPO), which exhibits a characteristic spectral change depending on the specific chemical modification induced by the ROS (Figure S10).[31,32] Only the characteristic EPR signal of DMPO-OOH was observed, providing clear evidence of $O_2^{\bullet-}$ generation. The concentration of $O_2^{\bullet-}$ was also dependent on the photo-irradiation time, ensuring that hPAG generated $O_2^{\bullet-}$ via electron transfer (Figure S10). Moreover, $OH^{\bullet}$ was not identified in hydroxyphenyl fluorescein (HPF) assay (Figure S11).

Additionally, the attenuated absorbance of ABDA was investigated to identify type II ROS ($^1O_2$) generated upon photo-irradiation of the polymer. While there was negligible $^1O_2$ generation from hPG, the absorbance of ABDA with hPAG was remarkably attenuated compared to that of s-hPAG (Figures 1b and S12b). Control experiments with diethanolamine (a fragment of hPAG) and BAG (monomer of hPAG) did not show significant changes in ABDA absorbance (Figure S13) relative to that of hPAG, and this establishes the importance of polymer networks for photo-induced ROS generation. The addition of NaN_3 as a $^1O_2$ scavenger successfully quenched the $^1O_2$ generated by hPAG, thus, changes in the absorbance of ABDA did not occur (Figure S12).[33] Moreover, we monitored the absorbance of ABDA using photo-activated hPAG at various pH because we assumed that the protonation state of a polymer could influence its interaction with O_2. The $^1O_2$ generation capability increased as the pH decreased from 11 to 7 to 3, and we correlated this to the enhanced interactions with O_2 upon the creation of positive charge and formation of hydrogen bond donor−protonated amine ($-NH_2^+-$) species under acidic conditions (Figure 1c). We further analyzed the $^1O_2$ generation

https://doi.org/10.1021/jacsau.2c00050
JACS Au 2022, 2, 933−942

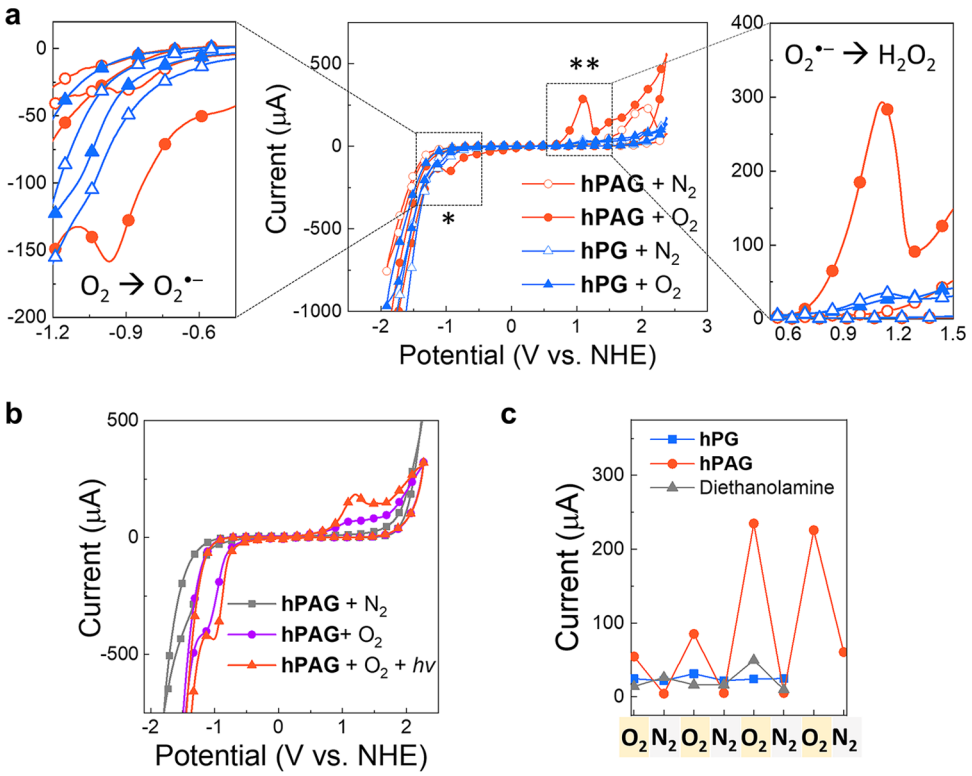

Figure 2. Evidence of electron transfer from the polymer to O_2. (a) Cyclic voltammetry (CV) curves of the aqueous polymer solution saturated with N_2 or O_2. Asterisks indicate the two different species of ROS generated by electron transfer. Current at +0.94 and −0.87 V (vs NHE) corresponds to $O_2^{\bullet-}$ → H_2O_2 (right) and O_2 → $O_2^{\bullet-}$ (left), respectively. (b) CV analysis of the effect of photo-irradiation on hPAG under different atmospheres. (c) Recording of peak oxidative current at +0.94 V upon cyclic bubbling of O_2 and N_2. Conditions: bubbling time = 20 min, scan rate = 50 mV/s, counter electrode = Pt, reference = Ag/AgCl (std. KCl), working electrode = polymer-coated FTO, and electrolyte = 0.1 M *t*-butylammonium hexafluorophosphate ($TBA^+PF_6^-$).

from hPAG using 2,2,6,6-tetramethylpiperidine (TEMP) by an EPR spin-trap method (Figure S14).[34] The generation of $^1O_2$ from hPAG is surprising because hPAG does not possess the appropriate energy bandgap (ca. 2.21 eV) to produce $^1O_2$ via the conventional energy transfer mechanism (type II) (Figure S6).[29] This suggests the possibility of an alternative mode for $^1O_2$ generation through $O_2^{\bullet-}$ via a sequential electron transfer cascade for O_2 (type I).[35,36] The $^1O_2$ generation pathway through electron transfer and further mechanistic analyses on hPAG and hPG are assessed in detail in later sections.

2.3. Electron Transfer from hPAG to Molecular Oxygen (O_2)

Cyclic voltammetry (CV) was used to examine the electron transfer from hPAG to produce $O_2^{\bullet-}$ using ferrocene as the external standard (+0.63 V vs NHE) (Figures 2 and S15).[37−39] To identify the ROS generated through electron transfer, current changes from hPAG and hPG under O_2 or N_2 bubbling were analyzed (Figure 2a). In contrast to the CV spectrum of hPAG under saturated N_2 conditions, new peaks at +0.94 and −0.87 V (vs NHE) appeared under saturated O_2 conditions under a negative sweep (reduction followed by oxidation). The potential for $O_2^{\bullet-}$ generation ranges from 0 to −1.0 V (vs NHE), depending on the electron donor.[37] Therefore, the peak at −0.87 V (marked with an asterisk) was consistent with the generation of $O_2^{\bullet-}$ from hPAG (Figure 2a, left). The other new peak at +0.94 V (double asterisks) indicates the conversion of $O_2^{\bullet-}$ to H_2O_2 (Figure 2a, right).[38,39] However, this peak did not appear under a positive sweep (oxidation followed by reduction) (Figure S16). This indicates that $O_2^{\bullet-}$ generation through reductive potential sweep must occur first for the conversion to H_2O_2. In addition, potential sweep with photo-irradiation resulted in much clearer peaks and higher current peaks at −0.87 and +0.94 V than that in the case without photo-irradiation, supporting the photo-activated generation of ROS (Figure 2b). No distinguishable current peak was observed under N_2 bubbling. Furthermore, we monitored the current recovery of the peak at +0.94 V under cyclic bubbling of O_2 and N_2; the current was found to be significantly altered for hPAG (Figures 2c and S17a), whereas hPG did not exhibit any change (Figures 2c and S17b). Diethanolamine, a simple fragment of hPAG, exhibited a slight current change under O_2 bubbling; however, its magnitude was considerably smaller than that of hPAG (Figure S17c). This result demonstrates that the electron transfer capability of hPAG is highly affected by the presence of O_2 and polymer network.

2.4. Density Functional Theory (DFT) Calculations for Establishing the Plausible Mechanism of $^1O_2$ Generation

To further understand the mechanism of $O_2^{\bullet-}$ and $^1O_2$ generation, we performed density functional theory (DFT) calculations for the natural transition orbitals (NTOs) of hPG-O_2 and hPAG-O_2 to clarify the electronic transitions.[40] The NTOs indicate that a hole orbital with *p*-orbital character localizes on an O atom for hPG and on a N atom for hPAG, while an electron orbital exhibits π^* character in O_2 (Figure 3a,b). This indicates that the transition occurs from the O atom of hPG or the N atom of hPAG to O_2, further supporting ROS generation.

Mixed-reference spin-flip time-dependent density functional theory (MR-SF-TDDFT) calculations were performed for a

https://doi.org/10.1021/jacsau.2c00050
JACS Au 2022, 2, 933−942

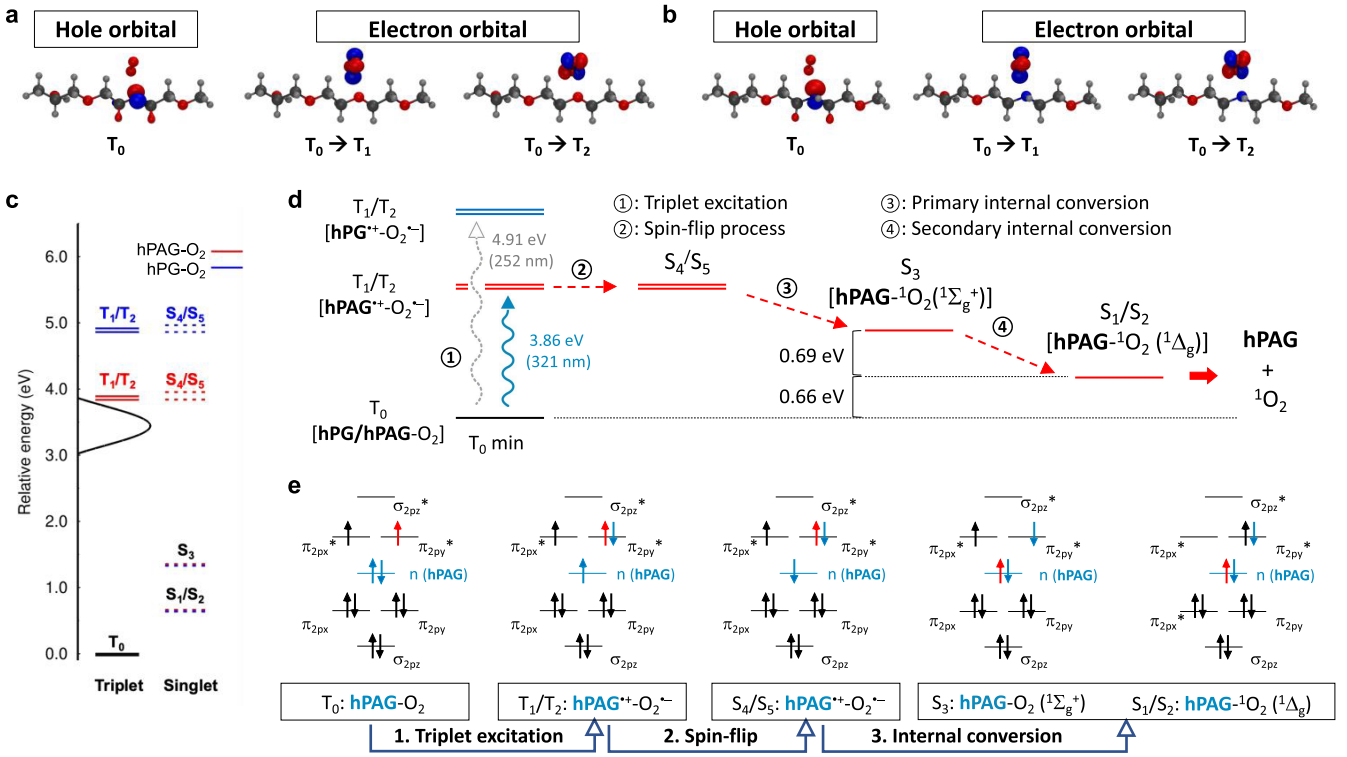

Figure 3. Density functional theory (DFT) calculations for analyzing $^1O_2$ generation properties of hPG and hPAG via spin-flip-based electron transfer. (a, b) Natural transition orbitals (NTOs) of (a) hPG-O_2 and (b) hPAG-O_2 at T_0 optimized geometry. Carbon, hydrogen, oxygen, and nitrogen in the molecular structure correspond to black, gray, red, and blue. (c) Relative energy diagram for singlet and triplet states in the minimum-energy structure of hPG-O_2 and hPAG-O_2 complexes at the triplet ground state (T_0) by mixed-reference spin-flip time-dependent density functional theory (MR-SF-TDDFT). The black Gaussian curve describes the incident photon energy band (λ = 360 nm with a bandwidth of 100 nm). (d) Process of $^1O_2$ generation by photo-activation. S_1 and S_2 states are degenerate, corresponding to the doubly degenerate singlet oxygen state ($^1\Delta_g$). Singlet states (S_1/S_2) for both complexes are 0.66 eV above T_0, almost identical to the T_0 and S_1 energy differences for isolated oxygen. The energy gap between S_3 and S_1/S_2 is 0.69 eV, which coincides with the energy gap between $^1\Delta_g$ and $^1\Sigma_g^+$ of isolated oxygen, implying that the S_3 state corresponds to the $^1\Sigma_g^+$ state of isolated oxygen. (e) Schematic illustration of molecular orbital configurations and overall transition for the singlet and triplet energy states. Blue spin represents the n lone pair electron from the nitrogen of hPAG. Red spin represents the electron from the π^* antibonding orbital of O_2.

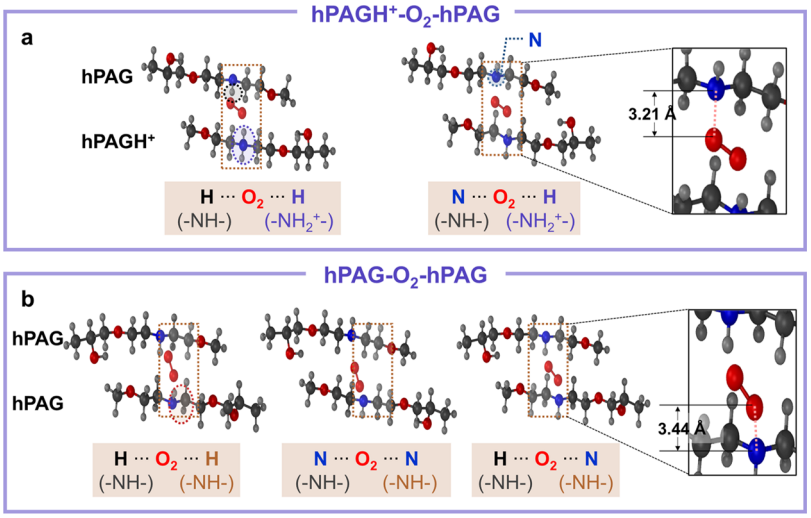

Figure 4. Close O_2 binding in the protonated hPAG network. (a) Molecular configurations of H−O_2−H and N−O_2−H in hPAGH$^+$ and hPAG, respectively. (b) Molecular configurations of H−O_2−H, N−O_2−N, and H−O_2−N in two hPAG fragments. The magnified structures in (a) and (b) show the lowest-energy structures of the hPAGH$^+$-O_2-hPAG and hPAG-O_2-hPAG configurations and interaction distance between O_2 and hPAG.

detailed photodynamic analysis of hPG and hPAG with O_2 (Figures 3c−e, S18, and Table S1).[41,42] The ground electronic states of hPG-O_2 and hPAG-O_2 have the T_0 state, where each π^* orbital of O_2 is singly occupied (Figure 3c,e). The two lowest triplet excited states (T_1/T_2) were nearly degenerate, corresponding to the charge transfer excitation from hPG/hPAG to the respective two π^* orbitals of O_2 (hPG/hPAG$^{\bullet+}$-$O_2^{\bullet-}$) (Figure 3c−e). Surprisingly, the $T_0 \rightarrow T_1$/T_2 transition energies

https://doi.org/10.1021/jacsau.2c00050
JACS Au 2022, 2, 933−942

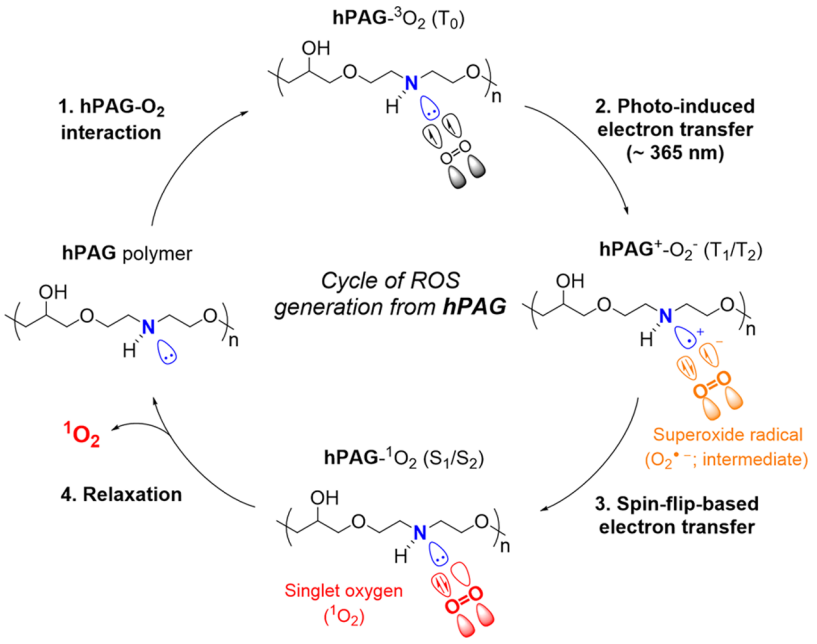

Figure 5. Plausible mechanism of $^1O_2$ generation via spin-flip-based electron transfer between hPAG and O_2.

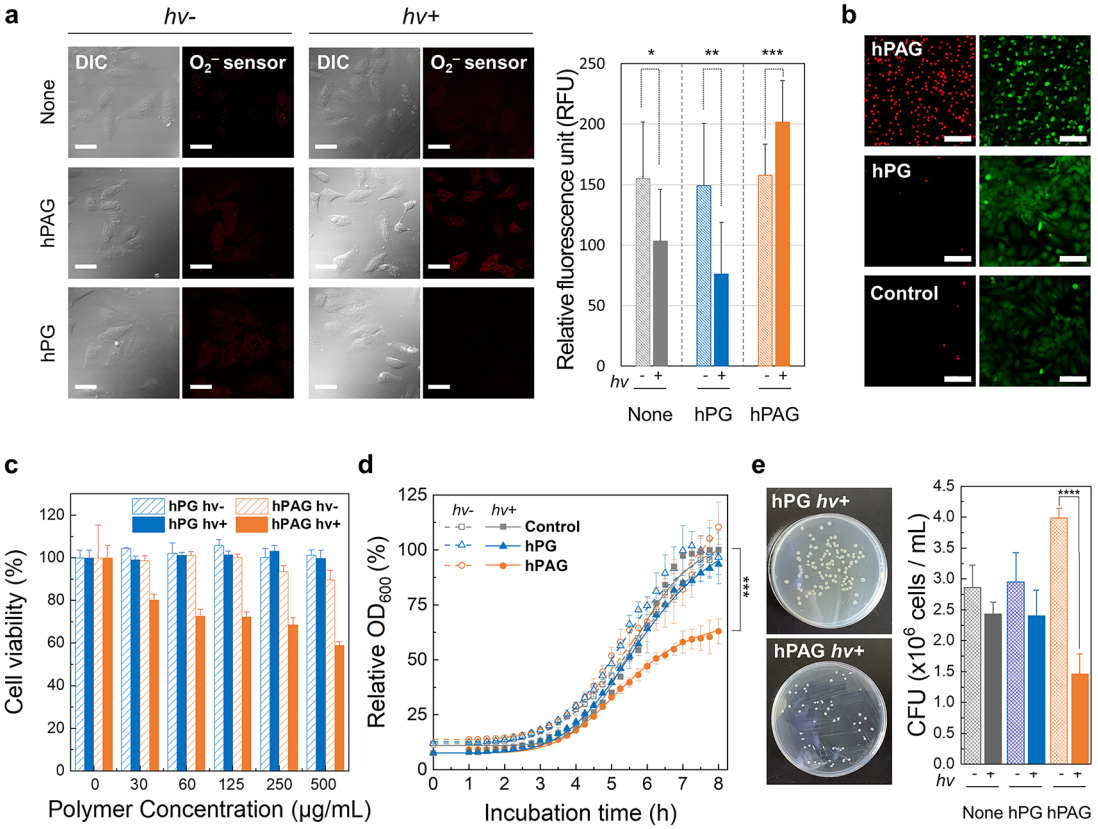

Figure 6. Intracellular $O_2^{\bullet -}$ and $^1O_2$ generation by spin-flip-based electron transfer and therapeutic applications. (a) Dihydroethidium (DHE) assay for $O_2^{\bullet -}$ and the fluorescence signal quantification for each condition (n = 9; three regions of interest (ROIs) from three different images). Scale bar = 40 μm. Data are presented as mean ± standard deviation, *p < 0.05, **p < 0.01. (b) Live/dead assay with Calcein-AM and propidium iodide (PI). Note that the green signals represent live cells, and the red signals represent dead cells. Scale bar = 100 μm. (c) Cell cytotoxicity of hPG and hPAG with or without photo-irradiation. Data are presented as mean ± standard deviation (n = 4). Conditions: 405 nm photoreactor, irradiation time = 600 s, light intensity = 28 mW/cm^2, total energy = 16.8 J/cm^2, and incubation time = 24 h. (d) Antimicrobial experiment of hPG and hPAG with or without photo-irradiation. (e) Colony visualization and quantification from antimicrobial experiment. Conditions: solar simulator irradiation time = 600 s, light intensity = 100 mW/cm^2, total energy = 60 J/cm^2, and incubation time for the colony formation unit (CFU) assay = 24 h. Data are presented as mean ± standard deviation (n = 3), *** p < 0.005, and **** p < 0.0005.

https://doi.org/10.1021/jacsau.2c00050
JACS Au 2022, 2, 933−942

for hPG and hPAG were substantially different (4.91 eV (252 nm) for hPG-O_2 and 3.86 eV (321 nm) for hPAG-O_2) and were consistent with the UV−vis absorption energy (Figure S5). The difference in excitation energies originates from the different orbital energies of the localized state of hPG and hPAG because electrons of the nitrogen atoms exhibit weaker electron−nuclear interactions than the electrons of the oxygen atoms, resulting in efficient electron transfer from the nitrogen atoms to O_2. In addition, hPAG exhibited a more stable oxidized state than hPG ($\Delta G^{\circ}_{hPG} - \Delta G^{\circ}_{hPAG} \approx 20$ kcal/mol), in agreement with the above-mentioned transition energy difference (4.91 vs 3.86 eV) (Figure S19).

Moreover, the singlet states of hPAG-O_2 complexes generated after the $T_0 \rightarrow T_1/T_2$ excitation were further evaluated to obtain mechanistic insights into this process (Figure 3d−e and Table S1). The S_4/S_5 states of the hPAG-O_2 complex are nearly degenerate, and their energies (3.89 eV) are very close to the T_1/T_2 energies (3.86 eV). Therefore, we can expect efficient intersystem crossing, which, in turn, enhances the spin-flip process to form the S_3/S_4 states after the triplet excitations (T_1/T_2, hPAG$^{\bullet+}$-$O_2^{\bullet-}$). Subsequently, these S_4/S_5 states undergo transition to the S_3 state (hPAG-$^1O_2(^1\Sigma_g)$) via internal conversion, followed by the generation of S_1/S_2 states (hPAG-$^1O_2(^1\Delta_g)$) (Figure 3d). Finally, $^1O_2$ is released in hPAG-$^1O_2(^1\Delta_g)$ state for a favorable energy state (Figure S20). The detailed electronic configurations of hPAG-O_2 are shown in Figure 3e.

Finally, to explain the origin of the improved ROS generation yield of hPAG under acidic conditions, we considered the optimized geometries of hPAGH$^+$-O_2-hPAG and hPAG-O_2-hPAG, where hPAGH$^+$ indicates hPAG bearing protonated nitrogen atoms (Figure 4 and Table S2). The H−O_2−H configuration depicts interacting O_2 intercalated between the protonated amines in hPAGH$^+$ and hydrogen of −NH− in hPAG (Figure 4a, left), while the N−O_2−H configuration depicts the interaction between the protonated amine in hPAGH$^+$ and the N lone pair in −NH− in hPAG (Figure 4a, right). In the hPAGH$^+$−O_2−hPAG network, the structure of N−O_2−H is more stable than that of H−O_2−H by −0.045 eV (Table S2). The hPAG-O_2-hPAG configurations are nearly degenerate, while the H−O_2−N configuration is the lowest-energy structure, with an energy of −0.005 eV (Figure 4b and Table S2). The complex system containing one hPAGH$^+$ has stronger binding with O_2 than that containing only hPAGs (Table S2). In the optimized geometry, moreover, the distance between the polymer backbone and O_2 of hPAGH$^+$-O_2-hPAG is 3.21 Å, which is shorter than that of hPAG-O_2-hPAG (3.44 Å) (Figure 4; magnified region). These results suggest that the origin of the improved ROS generation lies in the strong binding with O_2 under acidic conditions.

2.5. Suggested $^1O_2$ Generation Mechanism via Spin-Flip-Based Electron Transfer

A plausible mechanism for $^1O_2$ generation by the electron transfer cascade in the hPAG network with O_2 is depicted in Figure 5. (1) The nitrogen (N) of the hPAG polymer first interacts with the ground state oxygen under ambient conditions. (2) The photo-irradiation then induces charge separation in the network leading to the hPAG$^{\bullet+}$-$O_2^{\bullet-}$ conformation, a critical factor in the ROS generation. (3) The subsequent spin-flip process and primary/secondary internal conversions trigger the $O_2^{\bullet-}$-to-$^1O_2$ conversion. (4) $^1O_2$ is finally generated from the hPAG−$^1O_2$ complex by relaxation.

2.6. Photo-Induced Cancer Cell Death and Antimicrobial Activity by $^1O_2$ Generation

Type I ROS assay with 2′,7′-dichlorodihydrofluorescein diacetate (DCFH-DA) was performed to identify whether the ROS produced by the suggested mechanism can be applied in the intracellular environment.[43] Fluorescence enhancement after photo-irradiation was substantial for hPAG, whereas the change in fluorescence was negligible for hPG (Figure S21). Furthermore, an intracellular superoxide radical assay revealed stronger red fluorescence from hPAG than that from hPG upon photo-irradiation (Figure 6a). These results are in good agreement with those of the in vitro ROS assays.

In addition, cell death by photo-induced ROS was visualized by the live/dead and MTT-assays (Figure 6b,c). In the live/dead assay, red signals from dead cells were significant in the hPAG-treated cells upon photo-irradiation; however, the signal was not observed in the hPG-treated cells and negative control (Figure 6b). Additionally, we quantified the cell viability upon photo-irradiation for 10 min (light dose = 16.8 J/cm^2 with 405 nm LED array of 28 mW/cm^2 intensity; 60 J/cm^2 with solar simulator of 100 mW/cm^2) via the MTT assay (Figures 6c, S22, and Table S3). The viability of HeLa cells treated with hPAG (≥30 μg/mL) significantly decreased under light irradiation, while hPG did not exhibit a considerable change in cell viability.

Furthermore, the antimicrobial effect was assessed to confirm the $^1O_2$ generation by photo-activated hPAG (Figure 6d).[44] The bacterial growth, monitored by optical density measurement at 600 nm (OD_{600}), was significantly decelerated with hPAG under photo-irradiation. It was also visualized as colonies on an agar plate. The number of colonies with hPAG was less compared to that with hPG, and its quantification indicated that the ROS generation by hPAG could impede bacterial growth (Figure 6e).

Collectively, these results indicate that $^1O_2$ generation using this molecular design strategy based on O_2 interaction in the polymer network could be potentially applied to photodynamic therapy and antimicrobial effect.

3. CONCLUSIONS

In summary, we report a new $^1O_2$ generation process by the spin-flip-based electron transfer from an N-containing aliphatic polyglycerol-based polymer (hPAG) to O_2. The main $^1O_2$ generation process is related to the hyperbranched polymer network and a nitrogen atom, which strengthens O_2 interaction and stabilizes hPAG$^{\bullet+}$-$O_2^{\bullet-}$ (T_1/T_2 state). hPAG showed significant biocompatibility under dark conditions and induced cell death upon photo-irradiation. These results suggest that the ROS generation capability of hPAG via spin-flip-based electron transfer could induce the photo-dependent death of cancer cells and antimicrobial effect. The developed molecular design strategy for biocompatible and O_2-interactive photosensitizer is expected to contribute to the advancement of a new type of $^1O_2$ generator, and it might break the existing limitations of previous hydrophobic photosensitizers with a narrow range of applications.

■ ASSOCIATED CONTENT

Supporting Information

The Supporting Information is available free of charge at https://pubs.acs.org/doi/10.1021/jacsau.2c00050.

Materials and methods, and figures (^{1}H-NMR,^{13}C-NMR, UV−vis, photoluminescence, pH titration, ROS assays, cyclic voltammetry curves, DFT calculations, intracellular

https://doi.org/10.1021/jacsau.2c00050
JACS Au 2022, 2, 933−942

ROS assay, and cell cytotoxic assay) and tables of parameters from DFT calculation and cell cytotoxic assay (PDF)

AUTHOR INFORMATION

Corresponding Authors

Seung Kyu Min − *Department of Chemistry, Ulsan National Institute of Science and Technology (UNIST), Ulsan 44919, Republic of Korea;* orcid.org/0000-0001-5636-3407; Email: skmin@unist.ac.kr

Byeong-Su Kim − *Department of Chemistry, Yonsei University, Seoul 03722, Republic of Korea;* orcid.org/0000-0002-6419-3054; Email: bskim19@yonsei.ac.kr

Tae-Hyuk Kwon − *Department of Chemistry, Ulsan National Institute of Science and Technology (UNIST), Ulsan 44919, Republic of Korea; Center for Wave Energy Materials, Ulsan National Institute of Science and Technology (UNIST), Ulsan 44919, Republic of Korea;* orcid.org/0000-0002-1633-6065; Email: kwon90@unist.ac.kr

Authors

Jung Seung Nam − *Department of Chemistry, Ulsan National Institute of Science and Technology (UNIST), Ulsan 44919, Republic of Korea; Center for Wave Energy Materials, Ulsan National Institute of Science and Technology (UNIST), Ulsan 44919, Republic of Korea;* orcid.org/0000-0001-8557-131X

Youngjoo Hong − *Department of Chemistry, Yonsei University, Seoul 03722, Republic of Korea*

Chae Gyu Lee − *Department of Chemistry, Ulsan National Institute of Science and Technology (UNIST), Ulsan 44919, Republic of Korea; Center for Wave Energy Materials, Ulsan National Institute of Science and Technology (UNIST), Ulsan 44919, Republic of Korea*

Tae In Kim − *Department of Chemistry, Ulsan National Institute of Science and Technology (UNIST), Ulsan 44919, Republic of Korea*

Chaiheon Lee − *Department of Chemistry, Ulsan National Institute of Science and Technology (UNIST), Ulsan 44919, Republic of Korea; Center for Wave Energy Materials, Ulsan National Institute of Science and Technology (UNIST), Ulsan 44919, Republic of Korea*

Deok-Ho Roh − *Department of Chemistry, Ulsan National Institute of Science and Technology (UNIST), Ulsan 44919, Republic of Korea; Center for Wave Energy Materials, Ulsan National Institute of Science and Technology (UNIST), Ulsan 44919, Republic of Korea;* orcid.org/0000-0001-9871-4359

In Seong Lee − *Department of Chemistry, Ulsan National Institute of Science and Technology (UNIST), Ulsan 44919, Republic of Korea*

Songa Kweon − *Department of Chemistry, Ulsan National Institute of Science and Technology (UNIST), Ulsan 44919, Republic of Korea*

Gyunhyeok Ahn − *Department of Chemistry, Ulsan National Institute of Science and Technology (UNIST), Ulsan 44919, Republic of Korea;* orcid.org/0000-0001-7978-4984

Complete contact information is available at: https://pubs.acs.org/10.1021/jacsau.2c00050

Author Contributions

[‖]J.S.N., Y.H., C.G.L., and T.I.K. contributed equally to this work.

Funding

This work was supported by the Ulsan National Institute of Science & Technology (UNIST) (Research Fund 1.220026.01), and the National Research Foundation of Korea (NRF) (Grant 2016M1A2A2940910, 2017M3A7B4052802, 2017R1A2B3012148, 2018R1A5A1025208, 2019R1A2C1007744, 2021M3H4A1A0305139011, 2021R1A2C3004978, and 2021R1A2C2009504). C.G.L. and I.S.L. acknowledge support from the Global Ph.D. Fellowship Program through the NRF funded by the Ministry of Education (NRF-2018H1A2A1061237 and NRF-2017H1A2A1043792).

Notes

The authors declare no competing financial interest.

ACKNOWLEDGMENTS

J.S.N. is thankful for the support from the ASAN Foundation Biomedical Science Scholarship.

REFERENCES

(1) Wu, W.; Mao, D.; Xu, S.; Kenry; Hu, F.; Li, X.; Kong, D.; Liu, B. Polymerization-enhanced photosensitization. *Chem.* **2018**, *4*, 1937−1951.

(2) Hoffmann, N. Photochemical reactions as key steps in organic synthesis. *Chem. Rev.* **2008**, *108*, 1052−1103.

(3) Albeti, M. N.; Orfanopoulos, M. The cyclopropyl group as a hypersensitive probe in the singlet oxygen ene reaction mechanism. *Org. Lett.* **2008**, *10*, 2465−2468.

(4) Montagnon, T.; Tofi, M.; Vassilikogiannakis, G. Using singlet oxygen to synthesize polyoxygenated natural products from furans. *Acc. Chem. Res.* **2008**, *41*, 1001−1011.

(5) Bayer, P.; Schachtner, J.; Májek, M.; Wangelin, A. J. Visible light-mediated photo-oxygenation of arylcyclohexenes. *Org. Chem. Front.* **2019**, *6*, 2877−2883.

(6) Lan, M.; Zhao, S.; Liu, W.; Lee, C.-S.; Zhang, W.; Wang, P. Photosensitizers for photodynamic therapy. *Adv. Healthcare Mater.* **2019**, *8*, No. 190032.

(7) Dolmans, D. E.; Fukumura, D.; Jain, R. K. Photodynamic therapy for cancer. *Nat. Rev. Cancer* **2003**, *3*, 380−387.

(8) DeRosa, M. C.; Crutchley, R. J. Photosensitized singlet oxygen and its applications. *Coord. Chem. Rev.* **2002**, *233*−*234*, 351−371.

(9) Lovell, J. F.; Liu, T. W. B.; Chen, J.; Zheng, G. Activatable photosensitizers for imaging and therapy. *Chem. Rev.* **2010**, *110*, 2839−2857.

(10) Monro, S.; Colón, K. L.; Yin, H.; Roque, J., III; Konda, P.; Gujar, S.; Thummel, R. P.; Lilge, L.; Cameron, C. G.; McFarland, S. A. Transition metal complexes and photodynamic therapy from a tumor-centered approach: Challenges, opportunities, and highlights from the development of TLD1433. *Chem. Rev.* **2019**, *119*, 797−828.

(11) Nguyen, V.-N.; Yan, Y.; Zhao, J.; Yoon, J. Heavy-atom-free photosensitizers: from molecular design to applications in the photodynamic therapy of cancer. *Acc. Chem. Res.* **2021**, *54*, 207−220.

(12) Li, X.; Zheng, B.-D.; Peng, X.-H.; Li, S.-Z.; Ying, J.-W.; Zhao, Y.; Huang, J.-D.; Yoon, J. Phthalocyanines as medicinal photosensitizers: developments in the last five years. *Coord. Chem. Rev.* **2019**, *379*, 147−160.

(13) Chen, Y.-L.; Li, S.-W.; Chi, Y.; Cheng, Y.-M.; Pu, S.-C.; Yeh, Y.-S.; Chou, P.-T. Switching luminescent properties in osmium-based β-diketonate complexes. *ChemPhysChem* **2005**, *6*, 2012−2017.

(14) Wang, Z.; Ivanov, M.; Gao, Y.; Bussotti, L.; Foggi, P.; Zhang, H.; Russo, N.; Dick, B.; Zhao, J.; Donato, M. D.; Mazzone, G.; Luo, L.; Fedin, M. Spin-orbit charge-transfer intersystem crossing (ISC) in compact electron donor-acceptor dyads: ISC mechanism and application as novel and potent photodynamic therapy reagents. *Chem. - Eur. J.* **2020**, *26*, 1091−1102.

(15) Yogo, T.; Urano, Y.; Ishitsuka, Y.; Maniwa, F.; Nagano, T. Highly efficient and photostable photosensitizer based on BODIPY chromophore. *J. Am. Chem. Soc.* **2005**, *127*, 12162−12163.
(16) Marin, D. M.; Payerpaj, S.; Collier, G. S.; Ortiz, A. L.; Singh, G.; Jones, M.; Walter, M. G. Efficient intersystem crossing using singly halogenated carbomethoxyphenyl porphyrins measured using delayed fluorescence, chemical quenching, and singlet oxygen emission. *Phys. Chem. Chem. Phys.* **2015**, *17*, 29090−29096.
(17) Wang, X.; Song, Y.; Pan, G.; Han, W.; Wang, B.; Cui, L.; Ma, H.; An, Z.; Xie, Z.; Xu, B.; Tian, W. Exploiting radical-pair intersystem crossing for maximizing singlet oxygen quantum yields in pure organic fluorescent photosensitizers. *Chem. Sci.* **2020**, *11*, 10921−10927.
(18) Melle, S.; Calderón, O. G.; Laurenti, M.; Mendez-Gonzalez, D.; Egatz-Gómez, A.; López-Cabarcos, E.; Cabrera-Granado, E.; Díaz, E.; Rubio-Retama, J. Förster Resonance Energy Transfer Distance Dependence from Upconverting Nanoparticles to Quantum Dots. *J. Phys. Chem. C* **2018**, *122*, 18751−18758.
(19) Ibraev, N. K.; Seliverstova, E. V.; Artyukhov, V. Y. Dependence of the efficiency of triplet-triplet energy transfer on the distance between the donor and acceptor. *Russ. Phys. J.* **2015**, *57*, 1160−1164.
(20) Deng, H.; Li, Q.; Liu, J.; Wang, F. Active sites for oxygen reduction reaction on nitrogen-doped carbon nanotubes derived from polyaniline. *Carbon* **2017**, *112*, 219−229.
(21) Vélez-Fort, E.; Pallecchi, E.; Silly, M. G.; Bahri, M.; Patriarche, G.; Shukla, A.; Sirotti, F.; Ouerghi, A. Single step fabrication of N-doped graphene/Si_3N_4/SiC heterostructures. *Nano Res.* **2014**, *7*, 835−843.
(22) Ahn, G.; Kweon, S.; Yang, C.; Hwang, J. E.; Kim, K.; Kim, B.-S. One-pot synthesis of hyperbranched polyamines based on novel amino glycidyl ether. *J. Polym. Sci. Pol. Chem.* **2017**, *55*, 4013−4019.
(23) Liu, S. G.; Li, N.; Ling, Y.; Kang, B. H.; Geng, S.; Li, N. B.; Luo, G. Q. pH-mediated fluorescent polymer particles and gel from hyperbranched polyethylenimine and the mechanism of intrinsic fluorescence. *Langmuir* **2016**, *32*, 1881−1889.
(24) Tóth, V.; Hermann, P.; Végh, D.; Zelles, T.; Géczi, Z. Study of the intrinsic fluorescence of a highly branched cationic dendrimer, poly(ethyleneimine) (PEI). *Molecules* **2019**, *24*, 3690.
(25) Koper, G. J. M.; Borkovec, M. Proton binding by linear, branched, and hyperbranched polyelectrolytes. *Polymer* **2010**, *51*, 5649−5662.
(26) Benjaminsen, R. V.; Mattebjerg, M. A.; Henriksen, J. R.; Moghimi, S. M.; Andresen, T. L. The possible "proton sponge" effect of polyethylenimine (PEI) does not include change in lysosomal pH. *Mol. Therapy* **2013**, *21*, 149−157.
(27) von Harpe, A.; Petersen, H.; Li, Y.; Kissel, T. Characterization of commervially available and synthesized polyethylenimines for gene delivery. *J. Controlled Release* **2000**, *69*, 309−322.
(28) Nam, J. S.; Kang, M.-G.; Kang, J.; Park, S.-Y.; Lee, S. J. C.; Kim, H.-T.; Seo, J. K.; Kwon, O.-H.; Lim, M. H.; Rhee, H.-W.; Kwon, T.-H. Endoplasmic reticulum-localized iridium(III) complexes as efficient photodynamic therapy agents via protein modifications. *J. Am. Chem. Soc.* **2016**, *138*, 10968−10977.
(29) Henderson, L. M.; Chappell, J. B. Dihydrorhodamine 123: a fluorescent probe for superoxide generation? *Eur. J. Biochem.* **1993**, *217*, 973−980.
(30) Kuznetsova, N. A.; Gretsova, N. S.; Yuzhakova, O. A.; Negrimovskii, V. M.; Kaliya, O. L.; Luk'yanets, E. A. New reagents for determination of the quantum efficiency of singlet oxygen generation in aqueous media. *Russ. J. Gen. Chem.* **2001**, *71*, 36−41.
(31) Chen, M.; Xu, H.; Li, D.; Xia, D.; Zhang, X. Mechanism of heterogeneous activation of persulfate with FeOCl under visible light Irradiation. *J. Mater. Res.* **2018**, *33*, 3549−3558.
(32) Wang, J.; Tang, L.; Zeng, G.; Deng, Y.; Dong, H.; Liu, Y.; Wang, L.; Peng, B.; Zhang, C.; Chen, F. 0D/2D interface engineering of carbon quantum dots modified Bi_2WO_6 ultrathin nanosheets with enhanced photoacitivity for full spectrum light utilization and mechanism insight. *Appl. Cat. B: Environ.* **2018**, *222*, 115−123.
(33) Harbour, J. R.; Issler, S. L. Involvement of the azide radical in the quenching of singlet oxygen by azide anion in water. *J. Am. Chem. Soc.* **1982**, *104*, 903−905.
(34) Yadav, D. K.; Posipíšil, P. Evidence on the formation of singlet oxygen in the donor side photoinhibition of photosystem II: EPR spin-trapping study. *PLoS One* **2012**, *7*, No. e45883.
(35) Khan, A. U.; Kasha, M. Singlet molecular oxygen in the Haber-Weiss reaction. *Proc. Natl. Acad. Sci. U.S.A.* **1994**, *91*, 12365−12367.
(36) Miyamoto, S.; Martinez, G. R.; Medeiros, M. H. G.; Mascio, P. D. Singlet molecular oxygen generated by biological hydroperoxides. *J. Photochem. Photobiol. B* **2014**, *139*, 24−33.
(37) Doménech-Carbó, A.; Cebrián-Torrejón, G.; Montoya, N.; Ueberschaar, N.; Scotti, M. T.; Benfodda, Z.; Hertweck, C. Electrochemical monitoring of ROS generation by anticancer agents: the case of chartreusin. *RSC Adv.* **2017**, *7*, 45200−45210.
(38) Rao, P. S.; Hayon, E. Redox potentials of free radicals. IV. Superoxide and hydroperoxy radicals $^{\bullet}O_2^-$ and $^{\bullet}HO_2$. *J. Phys. Chem. A* **1975**, *79*, 397−402.
(39) Nonell, S.; Flors, C. *Singlet Oxygen: Applications in Biosciences and Nanosciences*; Krumova, K.; Cosa, G., Eds.; Royal Society of Chemistry: London, 2016; Vol. *1*, 3−21.
(40) Shao, Y.; Gan, Z.; Epifanovsky, E.; Gilbert, A. T. B.; Wormit, M.; Kussmann, J.; Lange, A. W.; Behn, A.; Deng, J.; Feng, X.; Ghosh, D.; Goldey, M.; Horn, P. R.; Jacobson, L. D.; Kaliman, I.; Khaliullin, R. Z.; Kuś, T.; Landau, A.; Liu, J.; Proynov, E. I.; Rhee, Y. M.; Richard, R. M.; Rohrdanz, M. A.; Steele, R. P.; Sundstrom, E. J.; Woodcock, H. L.; Zimmerman, P. M.; Zuev, D.; Albrecht, B.; Alguire, E.; Austin, B.; Beran, G. J. O.; Bernard, Y. A.; Berquist, E.; Brandhorst, K.; Bravaya, K. B.; Brown, S. T.; Casanova, D.; Chang, C.-M.; Chen, Y.; Chien, S. H.; Closser, K. D.; Crittenden, D. L.; Diedenhofen, M.; DiStasio, R. A.; Do, H.; Dutoi, A. D.; Edgar, R. G.; Fatehi, S.; Fusti-Molnar, L.; Ghysels, A.; Golubeva-Zadorozhnaya, A.; Gomes, J.; Hanson-Heine, M. W. D.; Harbach, P. H. P.; Hauser, A. W.; Hohenstein, E. G.; Holden, Z. C.; Jagau, T.-C.; Ji, H.; Kaduk, B.; Khistyaev, K.; Kim, J.; Kim, J.; King, R. A.; Klunzinger, P.; Kosenkov, D.; Kowalczyk, T.; Krauter, C. M.; Lao, K. U.; Laurent, A. D.; Lawler, K. V.; Levchenko, S. V.; Lin, C. Y.; Liu, F.; Livshits, E.; Lochan, R. C.; Luenser, A.; Manohar, P.; Manzer, S. F.; Mao, S.-P.; Mardirossian, N.; Marenich, A. V.; Maurer, S. A.; Mayhall, N. J.; Neuscamman, E.; Oana, C. M.; Olivares-Amaya, R.; O'Neill, D. P.; Parkhill, J. A.; Perrine, T. M.; Peverati, R.; Prociuk, A.; Rehn, D. R.; Rosta, E.; Russ, N. J.; Sharada, S. M.; Sharma, S.; Small, D. W.; Sodt, A.; Stein, T.; Stück, D.; Su, Y.-C.; Thom, A. J. W.; Tsuchimochi, T.; Vanovschi, V.; Vogt, L.; Vydrov, O.; Wang, T.; Watson, M. A.; Wenzel, J.; White, A.; Williams, C. F.; Yang, J.; Yeganeh, S.; Yost, S. R.; You, Z.-Q.; Zhang, I. Y.; Zhang, X.; Zhao, Y.; Brooks, B. R.; Chan, G. K. L.; Chipman, D. M.; Cramer, C. J.; Goddard, W. A.; Gordon, M. S.; Hehre, W. J.; Klamt, A.; Schaefer, H. F.; Schmidt, M. W.; Sherrill, C. D.; Truhlar, D. G.; Warshel, A.; Xu, X.; Aspuru-Guzik, A.; Baer, R.; Bell, A. T.; Besley, N. A.; Chai, J.-D.; Dreuw, A.; Dunietz, B. D.; Furlani, T. R.; Gwaltney, S. R.; Hsu, C.-P.; Jung, Y.; Kong, J.; Lambrecht, D. S.; Liang, W.; Ochsenfeld, C.; Rassolov, V. A.; Slipchenko, L. V.; Subotnik, J. E.; Van Voorhis, T.; Herbert, J. M.; Krylov, A. I.; Gill, P. M. W.; Head-Gordon, M. Advances in molecular quantum chemistry contained in the Q-Chem 4 program package. *Mol. Phys.* **2015**, *113*, 184−215.
(41) Lee, S.; Filatov, M.; Lee, S.; Choi, C. H. Eliminating spin-contamination of spin-flip time dependent density functional theory within linear response formalism by the use of zeroth-order mixed-reference (MR) reduced density matrix. *J. Chem. Phys.* **2018**, *149*, No. 104101.
(42) Lee, S.; Kim, E. E.; Nakata, H.; Lee, S.; Choi, C. H. Efficient implementations of analytic energy gradient for mixed-reference spin-flip time-dependent density functional theory (MRSF-TDDFT). *J. Chem. Phys.* **2019**, *150*, No. 184111.
(43) Lee, C.; Nam, J. S.; Lee, C. G.; Park, M.; Yoo, C.-M.; Rhee, H.-W.; Seo, J. K.; Kwon, T.-H. Analysing the mechanism of mitochondrial oxidation-induced cell death using a multifunctional iridium(III) photosensitiser. *Nat. Commun.* **2021**, *12*, No. 26.
(44) He, W.; Kim, H.-K.; Wamer, W. G.; Melka, D.; Callahan, J. H.; Yin, J.-J. Photogenerated charge carriers and reactive oxygen species in

https://doi.org/10.1021/jacsau.2c00050
JACS Au 2022, 2, 933−942

ZnO/Au hybrid nanostructures with enhanced photocatalytic and antibacterial activity. *J. Am. Chem. Soc.* **2014**, *136*, 750−757.

https://doi.org/10.1021/jacsau.2c00050
JACS Au 2022, 2, 933−942